MODELLISTICA E CALCOLO SCIENTIFICO

MOX

MODELING AND SCIENTIFIC COMPUTING

MOX-Report No. 17/2015

Computational comparison of aortic root stresses in presence of stentless and stented aortic valve bio-prostheses

Nestola, M.G.C.; Faggiano, E.; Vergara, C.; Lancellotti, R.M.;

Ippolito, S.; Filippi, S.; Quarteroni, A.; Scrofani, R.

Computational comparison of aortic root stresses in presence of stentless and stented aortic valve bio-prostheses

Maria Giuseppina Chiara Nestola[1], Elena Faggiano[2], Christian Vergara[3],
Rocco Michele Lancellotti[3], Sonia Ippolito[4], Simonetta Filippi[5],
Alfio Quarteroni[6], Roberto Scrofani[7]

April 9, 2015

[1] Nonlinear Physics and Mathematical Modeling Lab., Dipartimento di Ingegneria, Università Campus Bio-Medico di Roma, Italy, `m.nestola@unicampus.it`

[2] MOX, Dipartimento di Matematica, and LaBS, Dipartimento di Chimica, Materiali e Ingegneria Chimica "Giulio Natta", Politecnico di Milano, Italy, `elena.faggiano@gmail.com`

[3] MOX, Dipartimento di Matematica, Politecnico di Milano, Italy, `{christian.vergara,roccomichele.lancellotti}@polimi.it`

[4] Radiology Division, Ospedale L.Sacco, Milan, Italy, `ippolito.sonia@hsacco.it`

[5] Nonlinear Physics and Mathematical Modeling Lab., Dipartimento di Ingegneria, Università Campus Bio-Medico di Roma, Italy, and International Center for Relativistic Astrophysics Network - I.C.R.A.Net, `S.Filippi@unicampus.it`

[6] SB MATHICSE CMCS,EPFL, Lausanne, Switzerland, `alfio.quarteroni@epfl.ch`

[7] Cardio-surgery Division, Ospedale L.Sacco, Milan, Italy, `scrofani.roberto@hsacco.it`

Keywords: Stentless aortic prosthesis, fluid-structure interaction, geometry deflation

Abstract

We provide a computational comparison of the performance of stentless and stented aortic prostheses, in terms of aortic root displacements and internal stresses. To this aim, we consider three real patients; for each of them we draw the two prostheses configurations, which are characterized by different mechanical properties. Moreover, for each patient, we consider also the healthy configuration. For each scenario, we solve the fluid-structure interaction problem arising between blood and aortic root, through Finite Elements. The results show a better agreement between stentless and healthy displacements and stresses, with respect to the stented case.

1 Introduction

Aortic valve pathologies represent an important cause of morbidity and mortality in industrialized countries [43]. The aortic valve is located at the annulus of the aortic root, i.e. the early portion of the ascending aorta. The aortic root includes: (a) three little elliptical depressions, called *sinuses of Valsalva*, that are classified in left-coronary, right-coronary and non-coronary sinuses; (b) a collagenous annulus surrounding the valvular orifice; and (c) the sinotubular junction (STJ), representing the region where the normal tubular configuration of the aorta is attained. The aortic valve comprises three thin and flexible structures, the leaflets, which are shaped like triangles and attached to the fibrous annulus with a parabolic-like profile (see Figure 1).
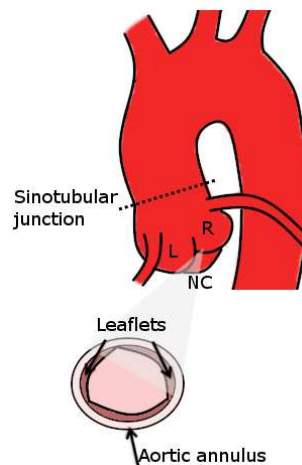

Figure 1: Gross anatomy of the aortic valve composed by the left (L), right (R), and non coronaric (NC) leaflet.

The efficient opening and closure of the aortic valve during the cardiac cycle guarantees the appropriate blood flow from the left ventricle to the ascending aorta, thus preventing regurgitation phenomena. The two main pathologies affecting the performance of the aortic valve are the *stenosis* and the *insufficiency*. The aortic stenosis occurs when the aortic valve narrows and fails to open totally. The narrowing obstructs the normal blood flow from the left ventricle into the aortic root, thus promoting an increase of the transvalvular pressure gradient (TPG) across the valve. High-pressure gradient stimulates a concentric hypertrophy of the left ventricle, i.e. the progressive thickening and stiffening of the ventricle walls, that may cause a reduction in the compliance of the ventricular cavity and, consequently, in the total volume of blood pumped by the heart to the systemic arteries [15]. In the aortic insufficiency the valve is incompetent and allows blood to flow passively back to the heart in the wrong direction during
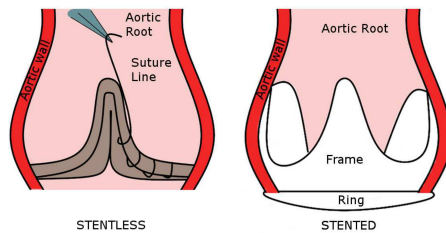
Figure 2: Simplified representation of the stentless (left) and stented (right) biological prostheses.

the diastolic phase. This incompetence can be due to a lesion of the semilunar leaflets or a damage of the aortic root which dilates, thus preventing the perfect closure of the aortic valve [53].

A native valve affected by a valvular pathology requires a surgical treatment in order to restore its physiological performance. The most common surgical treatment consists in the valve replacement through mechanical or biological tissue valves. In principle, the new implanted aortic valve should provide a hemodynamic pattern similar to the native one and a low thrombogenic risk in order to preempt the need for anticoagulants.

The classical biological prosthesis used to replace the aortic valve is the *stented* one, consisting of porcine aortic valve or pericardium bovine leaflets mounted on a polymeric frame (the stent) surrounded by a synthetic sewing ring. The stented prosthesis is implanted by suturing the synthetic ring to the aortic annulus (see Figure 2, right). More recently, starting from the late '80 of the previous century, a new type of bio-prosthesis has been considered, namely the *stentless* one. This is obtained from the stented prosthesis by eliminating the valvular sewing ring and the stent rigid support. In particular, the *Freedom Sorin SOLO* stentless prosthesis is constructed from two glutaraldehyde-treated bovine pericardial sheets without fabric reinforcement and without any other support. The design is created following the natural shape of the native aortic valve. This prosthesis requires a minimal invasive implantation procedure with a single suture line running around the three sinuses of Valsalva [10], see Figure 2, left. Clinical investigations comparing stented and stentless prostheses showed that the latter improves hemodynamic parameters in terms of pressure gradient, valve orifice area, and ventricle mass regression [10, 23].

In this contest, computational analyses based on the Finite Element Method may greatly contribute to investigate the performance of the biological prostheses, in terms of a quantification of stresses induced within the aortic root or hemodynamic patterns. In the literature several mechanical studies of stentless and stented aortic valve bio-prostheses were carried out both in idealized [14, 56, 2, 54] and in patient-specific [5, 4, 47] geometries. These works focused on

the analysis of the stress distribution in the valve leaflets and in the aortic root, thus ignoring the blood flow. Concerning the inclusion of the blood flow in the model, in [17] and [18] the authors studied the performance of the stented aortic prosthesis considering the three-dimensional fluid-structure interaction (FSI) arising between the leaflets and the blood (leaflet-blood interaction) while the aortic root was modeled as rigid. The same authors studied the stentless aortic prosthesis with a model that includes a complete FSI, thus also accounting for the interaction between the aortic wall and the blood (wall-blood interaction) [16] (see also [33, 35]). Due to the mathematical complexity of such models, these studies restricted their attention to an ideal axial symmetric geometry, assuming non physiological Reynolds number.

The aim of this work is to compare the performance of stentless and stented prostheses in terms of mechanical stresses induced within the aortic root wall by the blood. To do this, we performed a computational study based on wall-blood FSI simulations in real geometries. For each geometry, we drew the stented, the stentless, and the native configurations. The characterization of the three scenarios was based on a different choice of the structural properties of the aortic root, to account for the frame in the stented case and for the suture in the stentless one. To the best of our knowledge, this is the first attempt to compare the mechanical performance of stentless and stented biological prostheses using wall-blood FSI simulations in patient-specific geometries, with a detailed characterization of the mechanical behavior of the different region of the aortic root (native wall, rigid frame, sewing ring).

2   Material and methods

2.1   Patient dataset

Our dataset comprised three patients routinely referred to the Cardiac-Surgery Department of Ospedale Sacco, Milan, Italy, referred in what follows to as Patients 1, 2 and 3. Patients 1 and 2 featured a tricuspid aortic valve, whereas Patient 3 a bicuspid one. All the patients suffered from a calcific aortic valve stenosis confirmed by the elevated values of the transvalvular pressure gradient, see Table 1. Accordingly, they were subjected to a surgical treatment consisting in aortic valve replacement with the Freedom Sorin SOLO stentless biological prosthesis. Details about the demographic information of the three patients can be found in Table 1.

A Philips Brilliance CT 64-slice system was employed to perform a post-surgery three dimensional Contrast Enhanced Computed Tomography (3D-CE-CT) study with a slice thickness of $0.67\,mm$, a slice spacing of $0.33mm$, a reconstruction matrix of 512×512 pixels, and a final resolution of $0.45mm \times 0.45mm \times 0.33mm$. 3D-CE-CT images were acquired at different instants of the cardiac cycle. A CE-CT slice $3.74mm$ thick was then acquired in the valvular plane and a valvular in-plane image was reconstructed.

	Age	Sex	pre-operative TPG (mmHg)
Patient 1	33	M	68
Patient 2	65	M	52
Patient 3	84	M	44

Table 1: Demographic information for the three patients considered in the present study. TPG=tranvalvular pressure gradient.
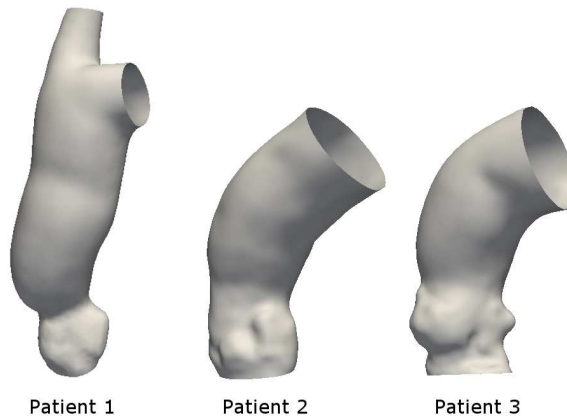

Figure 3: Lumen boundary surfaces reconstructed from CT images.

International Review Broad approval was obtained for the conduct of this study, and the board waived the need for patient consent.

2.2 Geometry reconstruction and mesh generation

To perform the reconstructions of the aortic geometries we started from the 3D-CE-CT scans corresponding to the diastolic phase. A surface model of the aortic root and ascending aorta was obtained for each patient using a level set-segmentation technique implemented in the Vascular Modeling Toolkit (vmtk, www.vmtk.org) [1]. This technique produces as output a surface representing the interface between the vessel lumen and the arterial wall. The surface was then cut at the aortic root inlet with a plane corresponding to the valvular one and at the outlets by planes perpendicular to the lumen longitudinal axis (see Figure 3). The internal volume of this surface, occupied by the fluid, was then discretized using tetrahedral mesh as in [24]. Moreover, a solid grid was obtained with the same tool. In particular, four layers of tetrahedra were generated via extrusion from the interface surface with a total wall thickness equal to 20% of the local vessel radius. Finally, we performed a mesh refinement of the fluid and wall meshes in the region of the aortic root in order to better capture the stress and the displacements distribution in this region (see Figure 4). For each
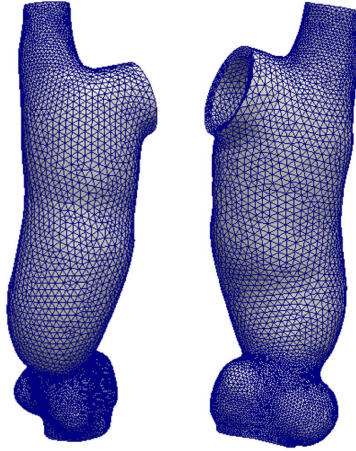
Figure 4: Fluid mesh (left) and structure mesh (right). Patient 1.

of the three patients, the final number of tetrahedra was about 3×10^5 for the fluid domain and about 1.9×10^5 for the solid domain. This mesh size was determined once the peak of the *Von Mises stresses* did not change by more than 4% between successive refinements (see Section 2.6 for the definition of the Von Mises stresses).

2.3   Characterization of the different scenarios

As discussed, our aim in this work was to compare the performance of the stentless and stented biological prostheses. To do this, for each patient we virtually designed the regions of the prostheses in contact with the aortic root (the frame for the stented case and the suture for the stentless case), and we selected different mechanical behavior in these regions with respect to the native wall. For any case, we assigned two of the four wall layers to the biological prosthesis and the remaining two to the aortic wall (see Figure 5).

Stented prosthesis
The stented prosthesis is composed of three elements (see Figure 2, right):

1. a flexible frame used as a skeleton and covered with a biocompatible material;

2. a base ring used to suture the prosthesis to the aortic annulus during the implantation;

3. the leaflets, made of pericardium bovine or obtained by using porcine aortic valve.
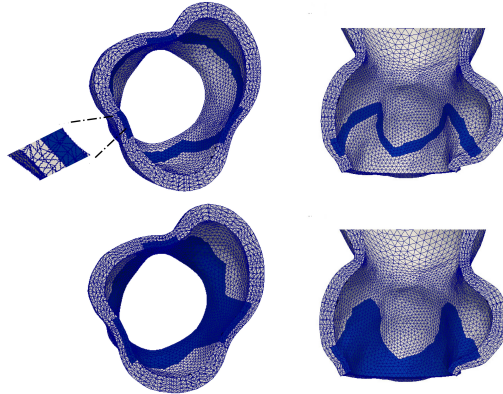
6

Figure 5: Aortic root in the stentless (up) and stented (bottom) configurations. In blue we depicted the regions characterized by different mechanical properties with respect to the native configuration. Patient 1.

We decided to model the flexible frame and the base ring as a homogeneous and isotropic structure inside the aortic root while we neglected the presence of the leaflets. As shown in Figure 5, bottom, the stented prosthesis has been modeled by reproducing the shape of the frame and of the sewing ring within the aortic root.

Stentless prosthesis
We considered the Freedom Sorin SOLO stentless prosthesis. In this case the valve is sutured directly to the aortic root without any frame, see Figure 2, left. Thus, we modeled the suture line running around the three sinuses of Valsalva as a homogeneous and isotropic structure inside the aortic root, and again we neglected the presence of the leaflets, see Figure 5, up. To obtain a patient-specific configuration of the suture, we drew the pattern of the suture in agreement with the patient-specific images.

Native aortic valve
In view of a complete comparison, we also considered for each patient the scenario representing the native case (also referred in what follows to as *healthy case*), obtained by considering constant-in-space parameters in all the aortic root. Again we neglected the presence of the leaflets.

 The values of the mechanical parameters used in the simulations are reported in Section 3.1. We point out that in our analysis the presence of the surgical wire used to suture the two prostheses to the aortic root was omitted. The choice of representing the three scenarios (stentless, stented, native) in the same geometry (although in fact all the patients have a stentless prosthesis) was aimed at

7

isolating the effect of the different biological prostheses, leaving unchanged all the other sources of perturbation (geometry, boundary conditions, etc).

Finally, we observe that in this work we decided to neglect the presence of the aortic leaflets and their opening-closure mechanism. This is of course a limitation and will be discussed in Sect. 4.1.

2.4 Including the diastolic pressure

In order to obtain meaningful numerical results, we needed to account for the diastolic pressure characterizing the reconstructed geometry. Indeed, in this work we considered a non-linear elastic material (see Section 2.5), so that we could not ignore the non-null diastolic blood pressure characterizing the radiological images used for the geometry reconstructions. To appropriately account for the blood pressure inside the diastolic geometry, one could introduce a pre-stress in the first Piola stress tensor [32], consider a modified updated Lagrangian formulation [26], or solve a backward elasto-dynamic problem [20, 44]. Here, we used the strategy introduced in [38] and [12]. In particular, the idea is to recover through the introduction of an inverse problem, the *zero-stress* geometry (that is the one one would have without the blood inside the lumen) by suitably deflating the diastolic one. Once this zero-stress geometry has been obtained, we were able to run our simulations using it as the reference configuration.

In particular, let $\mathcal{S}$ be the operator which, given a domain Ω_s and $P > 0$, returns the deformed configuration Ω_s^{FINAL} at the steady state of an unsteady structure problem, where Ω_s is the reference configuration and an uniform pressure P is exerted at the internal boundary. Homogeneous Dirichlet and Neumann conditions are prescribed at the artificial sections, introduced by the truncation of the domain, in the longitudinal and transversal directions, respectively. Thus, we have

$$\Omega_s^{FINAL} = \mathcal{S}(\Omega_s, P).$$

Now, call Ω_s^{DIAST} the diastolic structure domain obtained by extrusion of the diastolic fluid one. This configuration could be thought as the zero-stress one, Ω_s^{ZERO}, inflated by the diastolic pressure. In other terms, by setting $P^{DIAST} = 80\, mmHg$, we want to solve the following inverse problem:

Find Ω_s^{ZERO} such that $\Omega_s^{DIAST} = \mathcal{S}\left(\Omega_s^{ZERO}, P^{DIAST}\right).$

To solve this problem, we considered the following iterations

$$\Omega_{s,k}^{ZERO} = \Omega_{s,k-1}^{ZERO} + \alpha \left(\mathcal{S}\left(\Omega_{s,k-1}^{ZERO}, P^{DIAST}\right) - \Omega_{s,k-1}^{DIAST}\right),$$

for a suitable relaxation parameter $\alpha > 0$.

Once we obtained the zero-stress structure configuration Ω_s^{ZERO}, we built accordingly the zero-stress fluid domain which was then re-meshed with the same criteria used for the diastolic geometry.

2.5 Governing equations and numerical solution

Referring to Figure 6, left, let Ω_f be the current fluid domain. We considered the Navier-Stokes equations for an incompressible, homogeneous, Newtonian fluid, which is a good approximation to model the blood in the aorta, see e.g. [25]. Since the displacements are not negligible, we wrote these equations in the *Arbitrary Lagrangian-Eulerian* (ALE) configuration [34, 22], consisting in an arbitrary movement of the internal points of the fluid domain provided that they follow the interface displacement. In this work, we considered a harmonic extension to recover at each time step the points of the fluid domain.
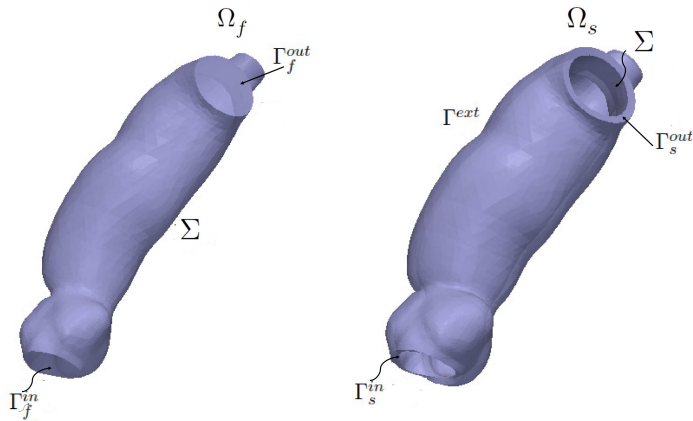

Figure 6: Computational domains. Fluid domain on the left, structure domain on the right.

Let Ω_s be the current structural domain, see Figure 6, right. For any function g defined in the current solid configuration, we denoted by $\widehat{g} := g \circ \mathcal{L}$ its counterpart in the reference domain Ω_s^0, where $\mathcal{L}$ is the Lagrangian map. We considered an elastic material and we wrote the unsteady elasto-dynamic problem written in the Lagrangian configuration.

The common current fluid-structure interface has been denoted by Σ.

Then, the differential formulation of the FSI problem reads as follows:

Find, at each time $t \in (0, T]$, fluid velocity $\boldsymbol{u}_f$, pressure p_f, structure displace-

ment $\boldsymbol{\eta}_s$ and fluid domain displacement $\boldsymbol{\eta}_m$, such that

$$
\begin{cases}
-\triangle\widehat{\boldsymbol{\eta}}_m = \mathbf{0} & \text{in } \Omega_f^0, \\
\widehat{\boldsymbol{\eta}}_m = \widehat{\boldsymbol{\eta}}_s & \text{at } \Sigma^0, \\
\rho_f \dfrac{D^A \boldsymbol{u}_f}{Dt} + \rho_f((\boldsymbol{u}_f - \boldsymbol{u}_m)\cdot\nabla)\boldsymbol{u}_f - \nabla\cdot\boldsymbol{T}_f(\boldsymbol{u}_f, p_f) = \mathbf{0} & \text{in } \Omega_f, \\
\nabla\cdot\boldsymbol{u}_f = 0 & \text{in } \Omega_f, \\
\boldsymbol{u}_f = \boldsymbol{g} & \text{at } \Gamma_f^{in}, \\
\dfrac{1}{|\Gamma_f^{out}|}\int_{\Gamma_f^{out}}(\boldsymbol{T}_f\,\boldsymbol{n})\cdot\boldsymbol{n}\,d\sigma - R_e\int_{\Gamma_f^{out}}\boldsymbol{u}_f\cdot\boldsymbol{n}\,d\sigma = P^{out} & \text{at } \Gamma_f^{out}, \\
\boldsymbol{u}_f = \dfrac{\partial\boldsymbol{\eta}_s}{\partial t} & \text{at } \Sigma, \\
\boldsymbol{T}_s(\boldsymbol{\eta}_s)\,\boldsymbol{n} - \boldsymbol{T}_f(\boldsymbol{u}_f, p_f)\,\boldsymbol{n} = \mathbf{0} & \text{at } \Sigma, \\
\rho_s \dfrac{\partial^2\widehat{\boldsymbol{\eta}}_s}{\partial t^2} - \nabla\cdot\widehat{\boldsymbol{T}}_s(\widehat{\boldsymbol{\eta}}_s) = \mathbf{0} & \text{in } \Omega_s^0, \\
\widehat{\boldsymbol{\eta}}_s = \mathbf{0} & \text{at } \Gamma_s^{in}\cup\Gamma_s^{out}, \\
\alpha_e\widehat{\boldsymbol{\eta}}_s + \widehat{\boldsymbol{T}}_s(\widehat{\boldsymbol{\eta}}_s)\,\widehat{\boldsymbol{n}} = \mathbf{0}, & \text{at } \Gamma^{0,ext}, \\
\end{cases}
\tag{1}
$$

and then find accordingly the fluid domain velocity $\widehat{\boldsymbol{u}}_m := \frac{\partial\widehat{\boldsymbol{\eta}}_m}{\partial t}$, and the new points $\boldsymbol{x}_f$ of the fluid domain by moving the points $\boldsymbol{x}_f^0$ of the reference domain Ω_f^0:

$$
\boldsymbol{x}_f = \boldsymbol{x}_f^0 + \widehat{\boldsymbol{\eta}}_m.
$$

In the previous coupled problem, $(1)_1$ represents the harmonic extension for the computation of the fluid domain, $(1)_{3-6}$ the fluid problem, and $(1)_{9-11}$ the structure problem. Moreover, μ is the constant blood viscosity, ρ_f and ρ_s the fluid and structure densities, $\boldsymbol{n}$ the unit normal exiting from the structure domain, $\frac{D^A}{Dt}$ the ALE derivative, $\boldsymbol{T}_f(\boldsymbol{u}_f, p_f) = \mu\left(\nabla\boldsymbol{u}_f + (\nabla\boldsymbol{u}_f)^T\right) - p\,\boldsymbol{I}$ the fluid Cauchy stress tensor, whereas $\widehat{\boldsymbol{T}}_s(\widehat{\boldsymbol{\eta}}_s)$ is the first Piola-Kirchhoff tensor for a nearly incompressible *exponential* material, that is

$$
\widehat{\boldsymbol{T}}_s(\boldsymbol{F}_s) = GJ_s^{-2/3}\left(\boldsymbol{F}_s - \frac{1}{3}\mathrm{tr}(\boldsymbol{F}_s^T\boldsymbol{F}_s)\boldsymbol{F}_s^{-\mathrm{T}}\right)e^{\gamma(J_s^{-\frac{2}{3}}\mathrm{tr}(\boldsymbol{F}_s^T\boldsymbol{F}_s)-3)} + \frac{\kappa}{2}\left(J_s - 1 + \frac{1}{J_s}\ln(J_s)\right)J_s\boldsymbol{F}_s^{-\mathrm{T}}.
\tag{2}
$$

Here $\boldsymbol{F}_s := \nabla_{\boldsymbol{x}_s^0}\boldsymbol{x}_s$, where $\boldsymbol{x}_s^0$ are the coordinates in the reference configuration and $\boldsymbol{x}_s$ those in the current configuration, $J_s := det(\boldsymbol{F}_s)$, κ is the *bulk modulus* and G the *shear modulus*. For small deformations this material behaves as a linear structure where the Poisson's ratio ν and the Young modulus E are related to κ and G as follows

$$
\kappa = \frac{E}{3(1-2\nu)}, \qquad G = \frac{E}{2(1+\nu)}.
\tag{3}
$$

The parameter γ characterizes the stiffness of the material for large displacements. Moreover, $\boldsymbol{T}_s(\boldsymbol{\eta}_s)$ is the Cauchy stress tensors of the solid. The exponential law to describe the aortic wall allows to account for the elastic behavior at very small displacements and for the strong stiffening due to collagen fibers for

higher deformations [30]. As for the artificial fluid sections, in $(1)_5$, $\boldsymbol{g}$ is a suitable velocity profile prescribed at the inlet, whereas in $(1)_6$, P^{out} is the external pressure and R_e is the resistance used to enforce absorbing boundary conditions at the fluid outlets, whose expression is given by [49] $R_e = \sqrt{\frac{\rho_f \tau}{2\sqrt{\pi}}} \frac{1}{A_0^{3/4}}$, with $\tau := \frac{E H_s \sqrt{\pi}}{(1-\nu^2)R^2}$, R being a representative radius of the outlet section, $A_0 = \pi R^2$, H_s a representative structure thickness at the outlet, and E and ν given by (3). At the structure artificial sections Γ_s^{in} and Γ_s^{out} we prescribed the homogeneous Dirichlet condition $(1)_{10}$: we kept the movement of inlets and outlets fixed. At the lateral structure surface Γ^{ext}, we prescribed the Robin condition $(1)_{11}$ to account for the elastic behavior of the surrounding tissue, characterized by the elastic parameter α_e [46].

At the FS interface, we wrote the matching conditions, which state the continuity of velocities $(1)_7$ and the continuity of tractions $(1)_8$ (*physical interface conditions*), whereas condition $(1)_2$ enforces the continuity of displacements (*geometrical interface condition*).

Finally, we observe that problem (1) has to be endowed with suitable initial conditions.

For the numerical solution of problem (1), after the time discretization, we considered at each time step the partitioned algorithm proposed in [50]. This is based on the application of the approximate-Newton method to the whole discretized-in-time FSI system, where the Jacobian is obtained by neglecting the shape derivatives and the geometrical coupling. This leads to a double-loop algorithm, where the geometrical coupling and the constitutive non-linearities are managed in the external iterations, whereas the physical coupling in the internal ones. To speed-up the computations, we considered an inexact variant of this scheme, obtained by performing at each time step only one external iteration. Thus, the geometrical coupling and the constitutive non-linearities are treated inexactly. On the contrary, the physical interface conditions $(1)_{7-8}$ were enforced exactly by using the *Robin-Robin* (RR) scheme proposed in [6], with the optimal coefficients α_f and α_s computed as proposed in [27]. The RR scheme has nice properties from the point of view of the convergnece, see [6, 7, 3, 48, 28]. This inexact scheme is accurate and stable for hemodynamic applications, see [50].

2.6   Computation of quantities of interest

To compare the performance of stentless and stented prostheses from the mechanical point of view, we focused on the tensional state of the aortic root. In particular, although we ran our simulations for all the heartbeat, we performed our analysis only at the systolic peak, when the valve is completely open.

We were interested in quantifying and comparing the different effects induced by the bio-prostheses on the aortic root wall, both in terms of displacements and internal stresses. To this aim, we evaluated for each case the dis-

placement $\boldsymbol{\eta}_s(t, \boldsymbol{x})$ obtained by our numerical simulations and in particular, given a volume of interest $\mathcal{V}$, we computed the average systolic displacement $\eta_s^{MEAN} = \|\boldsymbol{\eta}_s^{MEAN}\|_{\mathbb{R}^3}$, where $\eta_{s,i}^{MEAN} = \frac{1}{|\mathcal{V}|} \int_{\mathcal{V}} \eta_{s,i}(t_s, \boldsymbol{x})d\boldsymbol{x}$, and the maximum in space systolic displacement $\eta_s^{MAX} = \max_{\boldsymbol{x} \in \mathcal{V}} \|\boldsymbol{\eta}_s(t_s, \boldsymbol{x})\|_{\mathbb{R}^3}$, where t_s is the systolic instant.

We characterized the mechanical response of the aortic root also by computing the Von Mises stresses [40]. This is a quantity widely used in literature to predict yielding failure of ductile materials subject to any loading condition. Indeed, a yielding failure starts when the Von Mises stresses in a material reach the yield strength, which is the maximum permissible value deduced by uniaxial tensile tests. The Von Mises stresses $VM(t, \boldsymbol{x})$ are represented by a suitable scalar function given by a combination of the components of the Cauchy stress tensor. In particular, we have

$$VM = \sqrt{\frac{1}{2} \left((T_{s,11} - T_{s,22})^2 + (T_{s,33} - T_{s,22})^2 + (T_{s,11} - T_{s,33})^2 + 6 \left(T_{s,12}^2 + T_{s,23}^2 + T_{s,13}^2 \right) \right)},$$
$$(4)$$

where $T_{s,ij}$, $i, j = 1, 2, 3$, are the components of $\boldsymbol{T}_s$. Also in this case we introduced the average in space systolic Von Mises stresses, $VM^{MEAN} = \frac{1}{|\mathcal{V}|} \int_{\mathcal{V}} VM(t_s, \boldsymbol{x})d\boldsymbol{x}$, and the maximum in space systolic Von Mises stresses, $VM^{MAX} = \max_{\boldsymbol{x} \in \mathcal{V}} VM(t_s, \boldsymbol{x})$, as synthetic indicators in order to highlight the differences between stress distributions obtained for the stentless and stented prostheses.

3 Results

This section is divided into three parts. In the first one, we give some details about the numerical simulations. In the second part, we report a comparison among the three scenarios (healthy, stentless and stented) in terms of blood flow patterns in the aortic root, obtained by the FSI simulations. Finally, in the third part we discuss the results related to the vessel displacements and stresses, in particular to the quantities of interest introduced in Section 2.6.

3.1 Generalities of the numerical simulations

In all the numerical experiments of this work, we considered the nearly incompressible and isotropic exponential material described in Section 2.5. The values of the parameters involved in (2) are collected for the different materials in Table 2. For the choice of parameters E and ν we referred to the values reported in [36] for the healthy aortic wall, in [2] for the bovine pericardium prosthesis, and in [11, 45, 29, 55] for the rigid frame in the stented prosthesis. The corresponding values of the shear modulus G and of the bulk modulus κ were then computed by using equation (3). In addition, the value of γ was set in agreement with [31].

	$G\,[MPa]$	$\kappa\,[MPa]$	γ	$E\,[MPa]$	ν
healthy vessel	0.34	16.67	1	1	0.49
bovine pericardial sheet	1.34	66.67	1	4	0.49
rigid frame	3.70	11.11	1	10	0.35

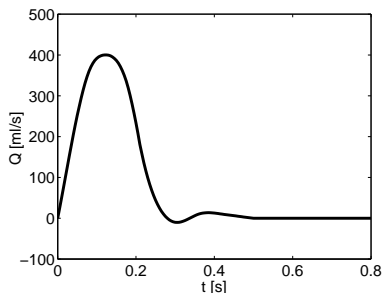Table 2: Values of material parameters adopted for the the numerical simulations.

Figure 7: Flow rate used to prescribe the velocity profile at the inlet of the fluid domain.

The material density ρ_s was assumed to be constant in each solid subdomain and equal to $1.1\,g\,cm^{-3}$, as well as the fluid density $\rho_f = 1.0\,g\,cm^{-3}$ and the dynamic viscosity $\mu = 0.035\,poise$. We also set in condition $(1)_{11}$ $\alpha_e = 500000\,dyne\,cm^{-3}$ [46] and $P^{out} = 80\,mmHg$ in condition $(1)_6$. These choices allowed to recover a pressure in the physiological range $(80 - 120\,mmHg)$.

At the inlet Γ_{in}^f of the fluid domain we prescribed a flat velocity profile for each of the three scenarios obtained by dividing the pulsatile flow rate shown in Figure 7 [51, 52] by the inlet section area. The unsteady numerical simulations were performed along the entire heart beat by using the parallel Finite Element Library LIFEV (www.lifeV.org). We used P1-P1 finite elements stabilized with the Interior Penalty technique [13] for the fluid problem and P1 finite elements for the structure problem.

We adopted the BDF1 scheme for the time integration of both the fluid and structure subproblems with a time step equal to $0.001\,s$.

In all the simulations of this work, the RR scheme converged without any relaxation, confirming its suitability for haemodynamic applications. The average number of RR iteration per time step was approximatively equal to 26 for all the three scenarios. At each RR iteration, we solved the linearized fluid and structure subproblems with the GMRes method and the harmonic extension with the Conjugate Gradient method, all preconditioned with an Additive-Two-Level Schwarz preconditioner, see [21] for further details.
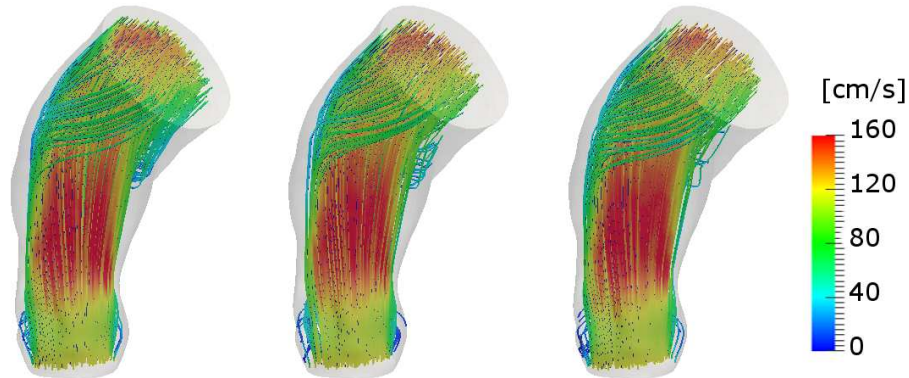
13

Figure 8: Peak systolic streamlines of the velocity field in the healthy (left), stentless (middle), and stented (right) scenarios for Patient 2.

3.2 Blood flow dynamics in the aortic root

In this work we performed unsteady numerical FSI simulations of a complete cardiac cycle. However, our analysis has been focused only at the systolic peak when the jet achieved its maximum strength and its influence on the arterial vessel is higher in terms of deformations and stresses. The systolic blood flow patterns obtained in the three scenarios are shown in Figure 8, which reported a representation of the systolic streamlines for the healthy (left), stentless (middle), and stented (right) scenarios of Patient 2. In this figure, one may clearly observe a fully developed jet with a maximum velocity of about $180\,cm\,s^{-1}$ formed downstream the aortic orifice, which remained confined to the core region of the aortic root for all the three scenarios. In this regard, we point out that a similar trend was reported in several experimental studies aimed at assessing the pattern of the velocity field in healthy control patients [8], and in both stentless and stented bio-prostheses [37, 42]. No substantial differences were noticed among the three scenarios. Similar patterns were also found in Patient 1 and Patient 3 (not shown).

3.3 Mechanical analysis of the aortic root

The mechanical analysis focused on the study of the spatial distribution of both displacements and stresses within the aortic root for the three scenarios (healthy, stentless and stented) and for each of the three patients. The aim was to compare the mechanical performance of the stentless and stented bio-prostheses with the one featured by the healthy case. The analysis was performed at systole when the blood pressure determined the highest mechanical displacements and stresses.

In Figure 9 we reported the volumes of interest $\mathcal{V}$ used for the computation of the synthetic quantities introduced in Section 2.6.

Figure 9: Representation of the volumes of interest $\mathcal{V}$ (in red) for Patient 1 (left), Patient 2 (middle), Patient 3 (right). Here L and R refer to the left-coronary and the right-coronary sinuses, respectively. The third sinus (the non-coronary sinus) is not visible.

3.3.1 Analysis of the aortic root displacements

Figure 10 shows the spatial distribution of the magnitude of the systolic displacement field $\eta(\boldsymbol{x}) = \|\boldsymbol{\eta}_s(t_s, \boldsymbol{x})\|_{\mathbb{R}^3}$ for all the patients in the three scenarios (healthy, stentless, and stented). The results obtained in all the three healthy configurations suggest an expansion of the aortic root conformed to experimental data (see the Discussion).

One may note that the stentless prosthesis allowed the aortic root to recover the healthy displacements, whereas the presence of the rigid frame in the stented one prevented the physiological dilation of the aortic root. To be more precise, in Table 3 we reported the values of the two quantities of interest η_s^{MEAN} and η_s^{MAX}, for all the performed simulations. These results confirmed the qualitative analysis suggested by Figure 10. Indeed, negligible differences were found between the values assumed in the stentless and healthy scenarios, whereas significant variations were found in the stented configuration. In particular, in this case the values of η_s^{MEAN} and η_s^{MAX} were about 20% lower than those computed in the physiological condition.

3.3.2 Analysis of Von Mises stresses in the aortic root

The spatial distributions of the systolic Von Mises stresses $VM(t_s, \boldsymbol{x})$ in the anterior and posterior internal wall of all the aortic roots are shown in Figure 11 and Figure 12, respectively. From these plots, we observe that in the three healthy cases the Von Mises stresses values were relatively low and uniformly distributed, in agreement with the results obtained in the existing literature.
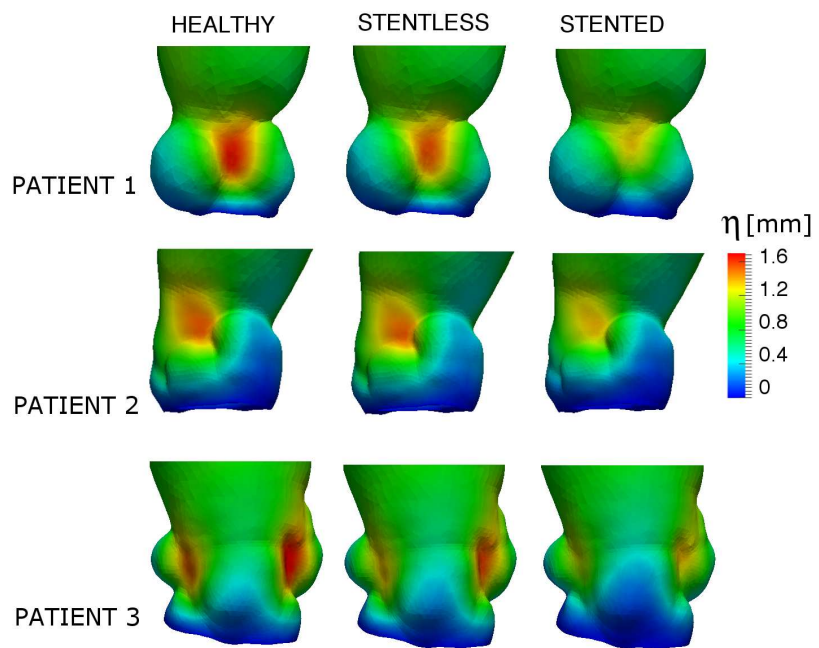
Figure 10: Spatial distribution at peak systole of the magnitude of the displacement field, η, in the aortic root of Patient 1, Patient 2 and Patient 3, respectively.

	Patient 1		Patient 2		Patient 3	
	η_s^{MAX}	η_s^{MEAN}	η_s^{MAX}	η_s^{MEAN}	η_s^{MAX}	η_s^{MEAN}
healthy	1.83	0.89	1.55	0.71	1.75	0.79
stentless	1.70	0.84	1.51	0.69	1.65	0.74
stented	1.49	0.71	1.30	0.59	1.38	0.61

Table 3: Values of η_s^{MAX} and η_s^{MEAN} at peak systole for all the cases. All the values are given in mm.

For example, the computational study in [9] suggested systolic VM stresses in the range $(140 - 200)\, kPa$, which fits very well with ours (see subfigures on the left in Figures 11 and 12). We also notice that in the stentless configurations these values are closer to the physiological level than in the stented models. In particular, we observe a complex and heterogeneous spatial stress distribution in the portion of the aortic root where the polymeric frame was placed. Additionally, in all the three stented configurations, the FSI simulations predicted multiple sites of stress concentrations, mainly localized in regions where change of curvature occurred.

A more quantitative analysis was performed by computing the values of VM^{MEAN} and VM^{MAX} for all the cases (see Table 4). We start analyzing Patients 1 and 2, since they featured similar results. First of all, we notice that both quantities assumed low values in the healthy scenarios. The stentless configurations revealed a slight increase in the values of VM^{MAX}, whereas the values of VM^{MEAN} were not significantly different from those obtained in the normal root. On the contrary, the stented scenario showed higher values of VM^{MAX} with respect to the healthy configuration. In particular, as shown in Figure 11 and Figure 12, the highest values of the Von Mises stresses occured in the region of the suture of the stentless prostheses. In the stented configuration, instead, the value of VM^{MAX} was found in the lower part of the non-coronary sinus in Patient 1 (see Figure 12) and between the right-coronary and the left-coronary sinuses in Patient 2 (see Figure 11).

	Patient 1		Patient 2		Patient 3	
	VM^{MAX}	VM^{MEAN}	VM^{MAX}	VM^{MEAN}	VM^{MAX}	VM^{MEAN}
healthy	165	67	169	59	152	56
stentless	202	66	192	56	230	55
stented	367	83	349	64	491	69

Table 4: Values of VM^{MAX} and VM^{MEAN} at peak systole for all the cases. All the values are given in kPa.

The stress distribution in Patient 3 showed notable differences with respect to the healthy case in both the stentless and stented configurations. In the suture region of the stentless prosthesis VM^{MAX} reaches a value 50% higher than the

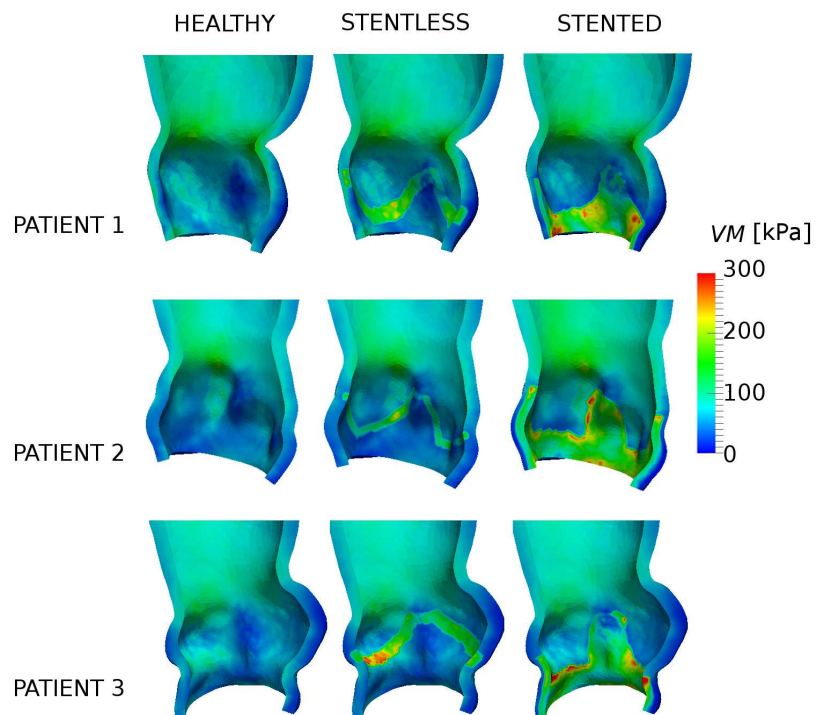Figure 11: Spatial distribution of the peak systolic Von Mises stresses $VM(t_s, \boldsymbol{x})$ in the anterior internal wall of the aortic root of Patient 1, Patient 2 and Patient 3, respectively.

Figure 12: Spatial distribution of the peak systolic Von Mises stresses $VM(t_s, \boldsymbol{x})$ in the posterior internal wall of the aortic root of Patient 1, Patient 2 and Patient 3, respectively.
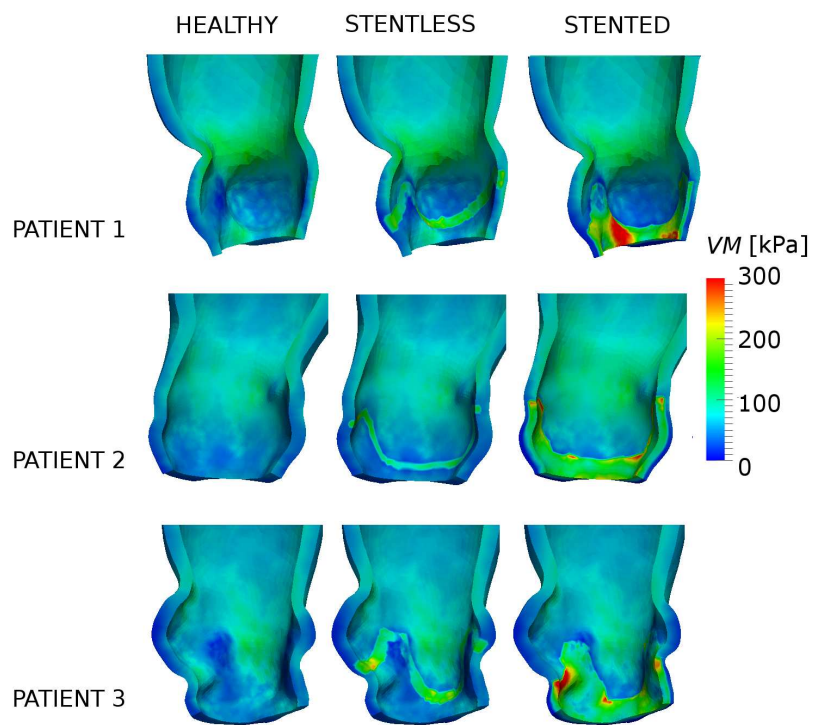
physiological level, see Figure 12. However, the FSI simulations predicted a more dramatic situation in the stented scenario. Indeed, in this case we observed a maximum stress concentration in the lower part of both the left and the right-coronary sinuses which assumed values 220% higher than in the physiological scenario (see Figure 11 and Figure 12).

4 Discussion

4.1 The choice of the computational model

In the last decades considerable attention has been paid to simulate the effect of the fluid-dynamics entering the ascending aorta on the aortic valve leaflets and/or the aortic root. One of the reasons for such an interest is the need of quantitative structural stress data to support the design of the prostheses commonly adopted in surgical practice.

In the literature different models have been considered so far in the context of both stentless and stented prostheses, depending on the focus of the study. Purely mechanical studies were carried out by using both idealized [14, 41, 2, 56] and patient specific geometries [5, 4, 47]. These works focused on the structural stresses in the valve leaflets and in the aortic root, but ignored the fluid-dynamics inside the root, and prescribed a physiological constant pressure at the internal structural boundary.

In [17, 18] the authors modeled the interaction between the blood fluid-dynamics and the leaflets under the assumption of rigid aortic root walls, to simulate the stented case, by using the *Fictitious Domain* method. They assumed an axi-symmetric hypothesis of the domain and a Reynolds number $Re = 900$ smaller than the physiological one.

In [16, 33, 35] the interaction with the compliant root to simulate the stentless case was accounted for in order to ensure an accurate modeling of the flow inside the aorta. Again, these works focused on simplified geometries and/or simplified flow assumptions.

Concerning the modeling of the prostheses, the frame of the stented one was either ignored [2] or included in the case of rigid aortic root [14, 17, 18]. The suture line in the stentless case was either ignored [5, 4, 16], or modeled with the same properties of the leaflets [56], or treated as a rigid material [33, 35].

In this context, the present work considered an FSI model between the blood and the aortic root, in order to compare the different wall stresses experienced by the aortic wall in the three different scenarios, namely the native, stentless, and stented ones. To perform this comparison, we assumed a different mechanical behavior for the different regions characterizing the prostheses. In particular, for the stented case we stiffened only the area in which the stent frame is actually sewn and not the entire aortic root as commonly done, whereas for the stentless case we considered a stiffening in the sewing ring (see Figure 5). This is an original contribution of the present work, indeed in the previous studies the

20

wall of the aortic root was assumed uniform to model both the stented and the stentless cases.

Another important feature of our model is the use of physiological geometrical and dynamic data to reproduce the three scenarios. Indeed, we used a non-linear model of finite elasticity to describe the aortic root dynamics and physiological fluid-dynamic boundary conditions which allowed to obtain physiological Reynolds numbers. Besides, we carried out our comparisons in real geometries reconstructed from CT images which have been suitably deflated to recover the zero-stress configuration. This is necessary to obtain significant results in presence of the finite elasticity. Although other works treated the problem of the geometry deflation (see, e.g., [32, 26, 20, 44, 12]), at the best of our knowledge, this is the first time that its application in a truely clinical context is addressed.

4.2 Mechanical performances of stentless and stented bio-prostheses and clinical implications

The primary goal of this work is to carry out a comparison of the mechanical performance of stentless and stented bio-prostheses. In view of a significant analysis, we considered, for each of the three patients, three configurations representing the stentless, the stented, and the healthy scenarios, respectively, which have been drawn in the same anatomical geometry, to make the comparison meaningful.

Although we performed unsteady numerical simulations along an entire heart beat, the analysis was carried out at the systole when the valve is completely open and the aortic root is subject to the highest mechanical solicitations due to the high values of the blood pressure. The mechanical response of each configuration was characterized by computing the spatial distribution of the magnitude of the displacement field and Von Mises stresses. In addition, in view of a synthetic quantitative comparison between the three scenarios, some indices were introduced by computing the average and the maximum values of the magnitude of the displacement field (η_s^{MEAN} and η_s^{MAX}) and of the Von Mises stresses (VM^{MEAN} and VM^{MAX}).

The discussion of the results of our study focuses on the following issues.

First, the results obtained in the healthy configuration showed a good agreement with the literature. In particular, in [19] the root dimensions at the level of the Valsalva sinuses and STJ were quantified by echocardiographic measurements, which revealed displacements of about $0.75\,mm$ (corresponding to a diameter variation of $1.5\,mm$), thus in agreement with our numerical results (see subfigures on the left in Figure 10). No measurements were obtained in that work at the commissures. Moreover, measurements on sheeps revealed a qualitative agreement of the systolic displacements with our results also at the commissures, in the sense that a greater displacement at these locations was observed in [39]. Finally, we point out that the Von Mises Stress values were in accordance with

the numerical results presented in [9].

The second and most relevant issue regards the significant differences observed by comparing the mechanical performances of the stentless and stented bio-prostheses, in terms of both displacements and stresses spatial distribution. In particular, the presence of the rigid frame in the stented scenarios caused a reduction of about 20% in the values of η_s^{MEAN} and η_s^{MAX} with respect to that of the healthy situation. On the contrary, negligible differences were observed between the stentless and the healthy configurations. Such a trend was also confirmed by computing the Von Mises Stress spatial distribution and the values of both the VM^{MEAN} and VM^{MAX} indices. In this case, very high stress values were found in all the stented configurations and especially in Patient 3 where VM^{MAX} increased by 220% with respect to the corresponding healthy scenario. Again, negligible differences (especially for Patients 1 and 2) were observed between the stentless and the healthy scenarios. Consequently, as a first immediate clinical implication of the results here presented, we point out that the stentless bio-prostheses seems to recover a more physiological dynamics, thus in principle improving the mechanical performance with respect to the stented ones.

The third important issue of our study regards the clinical implication related to the placement of the suture of the stentless prosthesis on the aortic root. Indeed, we found elevated Von Mises stresses for Patient 3 in correspondence of the change of curvature at the Valsalva sinuses, where the suture has been placed (remember that the stentless configurations are the real ones and that the sewing ring have been drawn following the radiological images). Instead, for Patients 1 and 2 where the sewing ring has been placed below the region of curvature changes, we found low stress values, comparable with the healthy ones. This suggests that the placement of the sewing ring may provide a better recovery of the physiological mechanical behavior.

4.3   Limitations

This work suffers of some limitations. Above all, we have neglected the presence of the leaflets and their mechanism of opening/closure. We believe, however, that in view of the preliminary comparison reported in this work, the inclusion of the leaflets, although providing more accurate results, could be neglected because of its low impact when comparing mechanical quantities in the aortic root wall, rather than in the leaflets. Moreover, we were interested in analyzing some quantities at the systole, when the leaflets are completely open. We observed from our results a fully developed jet downstream the aortic orifice, which remained confined to the core region of the aortic root, in agreement with experimental findings for stentless and stented bio-prostheses [37, 42]. Such an agreement demonstrated that our numerical models were able to capture the main features of the blood flow dynamics in the aortic root and for this reason we believe that the mechanism of opening/closing could be ignored for our purposes.

In any case, all of the three scenarios were characterized by the same limitation, so that in view of a comparison this simplifying choice should lead to small perturbations.

Another limitation consisted in the use of non-patient-specific (although physiological) flow boundary condition at the inlet of the computational domain. However, we believe that this simplification would not significantly change the conclusions of the present work.

References

[1] Luca Antiga, Marina Piccinelli, Lorenzo Botti, Bogdan Ene-Iordache, Andrea Remuzzi, and David A Steinman. An image-based modeling framework for patient-specific computational hemodynamics. *Medical & biological engineering & computing*, 46(11):1097–1112, 2008.

[2] G Arcidiacono, A Corvi, and T Severi. Functional analysis of bioprosthetic heart valves. *Journal of biomechanics*, 38(7):1483–1490, 2005.

[3] M. Astorino, F. Chouly, and M. Fernández. Robin based semi-implicit coupling in fluid-structure interaction: stability analysis and numerics. *SIAM Journal on Scientific Computing*, 31(6):4041–4065, 2009.

[4] F Auricchio, M Conti, A Ferrara, S Morganti, and A Reali. Patient-specific simulation of a stentless aortic valve implant: the impact of fibres on leaflet performance. *Computer methods in biomechanics and biomedical engineering*, 17(3):277–285, 2014.

[5] F Auricchio, M Conti, S Morganti, and P Totaro. A computational tool to support pre-operative planning of stentless aortic valve implant. *Medical engineering & physics*, 33(10):1183–1192, 2011.

[6] S. Badia, F. Nobile, and C. Vergara. Fluid-structure partitioned procedures based on Robin transmission conditions. *Journal of Computational Physics*, 227:7027–7051, 2008.

[7] S. Badia, F. Nobile, and C. Vergara. Robin-Robin preconditioned Krylov methods for fluid-structure interaction problems. *Computer Methods in Applied Mechanics and Engineering*, 198(33-36):2768–2784, 2009.

[8] Alex J Barker, Craig Lanning, and Robin Shandas. Quantification of hemodynamic wall shear stress in patients with bicuspid aortic valve using phase-contrast mri. *Annals of biomedical engineering*, 38(3):788–800, 2010.

[9] W Becker, J Rowson, JE Oakley, A Yoxall, G Manson, and K Worden. Bayesian sensitivity analysis of a model of the aortic valve. *Journal of biomechanics*, 44(8):1499–1506, 2011.

[10] Sven Beholz, Benjamin Claus, Simon Dushe, and Wolfgang Konertz. Operative technique and early hemodynamic results with the freedom solo valve. *JOURNAL OF HEART VALVE DISEASE*, 15(3):429, 2006.

[11] Gillian M Bernacca, Bernard OConnor, David F Williams, and David J Wheatley. Hydrodynamic function of polyurethane prosthetic heart valves: influences of young's modulus and leaflet thickness. *Biomaterials*, 23(1):45–50, 2002.

[12] J. Bols, J. Degroote, B. Trachet, B. Verhegghe, P. Segers, and J. Vierendeels. A computational method to assess the in vivo stresses and unloaded configuration of patient-specific blood vessels. *Journal of Computational and Applied Mathematics*, 246:10–17, 2013.

[13] E. Burman and P. Hansbo. Edge stabilization for the generalized Stokes problem: a continuous interior penalty method. *Computer Methods in Applied Mechanics and Engineering*, 195:2393–2410, 2006.

[14] G Cacciola, GWM Peters, and PJG Schreurs. A three-dimensional mechanical analysis of a stentless fibre-reinforced aortic valve prosthesis. *Journal of Biomechanics*, 33(5):521–530, 2000.

[15] SW Davies, AH Gershlick, and R Balcon. Progression of valvar aortic stenosis: a long-term retrospective study. *European heart journal*, 12(1):10–14, 1991.

[16] J De Hart, FPT Baaijens, GWM Peters, and PJG Schreurs. A computational fluid-structure interaction analysis of a fiber-reinforced stentless aortic valve. *Journal of biomechanics*, 36(5):699–712, 2003.

[17] J De Hart, GWM Peters, PJG Schreurs, and FPT Baaijens. A three-dimensional computational analysis of fluid–structure interaction in the aortic valve. *Journal of biomechanics*, 36(1):103–112, 2003.

[18] J De Hart, GWM Peters, PJG Schreurs, and FPT Baaijens. Collagen fibers reduce stresses and stabilize motion of aortic valve leaflets during systole. *Journal of biomechanics*, 37(3):303–311, 2004.

[19] Ruggero De Paulis, Giovanni Maria De Matteis, Paolo Nardi, Raffaele Scaffa, Maria Michaela Buratta, and Luigi Chiariello. Opening and closing characteristics of the aortic valve after valve-sparing procedures using a new aortic root conduit. *The Annals of thoracic surgery*, 72(2):487–494, 2001.

[20] S. de Putter, B.J.B.M. Wolters, M.C.M. Rutten, M. Breeuwer, F.A. Gerritsen, and F.N. van de Vosse. Patient-specific initial wall stress in abdominal aortic aneurysms with a backward incremental method. *Journal of Biomechanics*, 40:10811090, 2007.

[21] S. Deparis, G. Grandperrin, and A. Quarteroni. Parallel preconditioners for the unsteady navierstokes equations and applications to hemodynamics simulations. *Computer & Fluids*, 92:253–273, 2014.

[22] J. Donea. An arbitrary Lagrangian-Eulerian finite element method for transient dynamic fluid-structure interaction. *Computer Methods in Applied Mechanics and Engineering*, 33:689–723, 1982.

[23] J Dunning, RJ Graham, J Thambyrajah, MJ Stewart, SWH Kendall, and S Hunter. Stentless vs. stented aortic valve bioprostheses: a prospective randomized controlled trial. *European heart journal*, 28(19):2369–2374, 2007.

[24] Elena Faggiano and Luca Antiga. An open-source tool for patient-specific fluid-structure vessel mesh generation. In preparation.

[25] Luca Formaggia, Alfio M Quarteroni, and Alessandro Veneziani. *Cardiovascular mathematics*. Number CMCS-BOOK-2009-001. Springer, 2009.

[26] M.W. Gee, C. Reeps, H.H. Eckstein, and W.A. Wall. Prestressing in finite deformation abdominal aortic aneurysm simulation. *Journal of Biomechanics*, 42:1732–1739, 2009.

[27] Luca Gerardo-Giorda, Fabio Nobile, and Christian Vergara. Analysis and optimization of robin-robin partitioned procedures in fluid-structure interaction problems. *SIAM Journal on Numerical Analysis*, 48(6):2091–2116, 2010.

[28] G. Gigante and C. Vergara. Analysis and optimization of the generalized schwarz method for elliptic problems with application to fluid-structure interaction. *Numer Math. DOI:10.1007/s00211-014-0693-2*, 2014.

[29] K Jane Grande-Allen, Richard P Cochran, Per G Reinhall, and Karyn S Kunzelman. Finite-element analysis of aortic valve-sparing: influence of graft shape and stiffness. *Biomedical Engineering, IEEE Transactions on*, 48(6):647–659, 2001.

[30] G.A. Holzapfel and R.W. Ogden. Constitutive modelling of arteries. *Proc. R. Soc. Lond. Ser. A Math. Phys. Eng. Sci.*, 466(2118):1551–1596, 2010.

[31] CO Horgan and G Saccomandi. A description of arterial wall mechanics using limiting chain extensibility constitutive models. *Biomechanics and modeling in mechanobiology*, 1(4):251–266, 2003.

[32] M.-C. Hsu and Y. Bazilevs. Blood vessel tissue prestress modeling for vascular fluidstructure interaction simulation. *Finite Elements in Analysis and Design*, 47:593599, 2011.

[33] Ming-Chen Hsu, David Kamensky, Yuri Bazilevs, Michael S Sacks, and Thomas JR Hughes. Fluid–structure interaction analysis of bioprosthetic heart valves: significance of arterial wall deformation. *Computational Mechanics*, 54(4):1055–1071, 2014.

[34] T. J. R. Hughes, W. K. Liu, and T. K. Zimmermann. Lagrangian-Eulerian finite element formulation for incompressible viscous flows. *Computer Methods in Applied Mechanics and Engineering*, 29(3):329–349, 1981.

[35] David Kamensky, Ming-chen Hsu, Dominik Schillinger, John A Evans, Ankush Aggarwal, Michael S Sacks, Thomas J. R. Hughes, and Reference David Kamensky. A variational immersed boundary framework for fluid structure interaction : Isogeometric implementation and application to bioprosthetic heart valves. *ICES REPORT 14-12*, (May), 2014.

[36] TM Koch, BD Reddy, P Zilla, and T Franz. Aortic valve leaflet mechanical properties facilitate diastolic valve function. *Computer methods in biomechanics and biomedical engineering*, 13(2):225–234, 2010.

[37] John-Peder Escobar Kvitting, Petter Dyverfeldt, Andreas Sigfridsson, Stefan Franzén, Lars Wigström, Ann F Bolger, and Tino Ebbers. In vitro assessment of flow patterns and turbulence intensity in prosthetic heart valves using generalized phase-contrast mri. *Journal of Magnetic Resonance Imaging*, 31(5):1075–1080, 2010.

[38] R. M. Lancellotti. *Numerical Computations of Deflated Vascular Geometries fo Fluid-Structure Interaction in Haemodynamics.* PhD thesis, Universit degli Studi di Napoli Federico II, July 2012.

[39] E Lansac, HS Lim, Y Shomura, KH Lim, NT Rice, W Goetz, C Acar, and CMG Duran. A four-dimensional study of the aortic root dynamics. *European journal of cardio-thoracic surgery*, 22(4):497–503, 2002.

[40] F.A. Leckie and D.J. Bello. *Strength and Stiffness of Engineering Systems.* Springer, 2009.

[41] J Li, XY Luo, and ZB Kuang. A nonlinear anisotropic model for porcine aortic heart valves. *Journal of biomechanics*, 34(10):1279–1289, 2001.

[42] WL Lim, YT Chew, TC Chew, and HT Low. Pulsatile flow studies of a porcine bioprosthetic aortic valve in vitro: Piv measurements and shear-induced blood damage. *Journal of biomechanics*, 34(11):1417–1427, 2001.

[43] Donald Lloyd-Jones, Robert J Adams, Todd M Brown, Mercedes Carnethon, Shifan Dai, Giovanni De Simone, T Bruce Ferguson, Earl Ford, Karen Furie, Cathleen Gillespie, et al. Heart disease and stroke statistics2010 update a report from the american heart association. *Circulation*, 121(7):e46–e215, 2010.

[44] J. Lu, X. Zhou, and M. Raghavan. Inverse elastostatic stress analysis in pre-deformed biological structures: demonstration using abdominal aortic aneurysms. *Journal of Biomechanics*, 40:693696, 2007.

[45] TG Mackay, DJ Wheatley, GM Bernacca, AC Fisher, and CS Hindle. New polyurethane heart valve prosthesis: design, manufacture and evaluation. *Biomaterials*, 17(19):1857–1863, 1996.

[46] P. Moireau, N. Xiao, M. Astorino, C. A. Figueroa, D. Chapelle, C. A. Taylor, and J.-F. Gerbeau. External tissue support and fluidstructure simulation in blood flows. *Biomechanics and Modeling in Mechanobiology*, 11(1-2):1–18, 2012.

[47] S Morganti, M Conti, M Aiello, A Valentini, A Mazzola, A Reali, and F Auricchio. Simulation of transcatheter aortic valve implantation through patient-specific finite element analysis: Two clinical cases. *Journal of biomechanics*, 47(11):2547–2555, 2014.

[48] F. Nobile and C. Vergara. Partitioned algorithms for fluid-structure interaction problems in haemodynamics. *Milan Journal of Mathematics*, 80(2):443–467, 2012.

[49] Fabio Nobile, Matteo Pozzoli, and Christian Vergara. Time accurate partitioned algorithms for the solution of fluid–structure interaction problems in haemodynamics. *Computers & Fluids*, 86:470–482, 2013.

[50] Fabio Nobile, Matteo Pozzoli, and Christian Vergara. Inexact accurate partitioned algorithms for fluid-structure interaction problems with finite elasticity in haemodynamics. *Journal of Computational Physics*, 273:598–617, 2014.

[51] Sarah Nordmeyer, Eugénie Riesenkampff, Daniel Messroghli, Siegfried Kropf, Johannes Nordmeyer, Felix Berger, and Titus Kuehne. Four-dimensional velocity-encoded magnetic resonance imaging improves blood flow quantification in patients with complex accelerated flow. *Journal of Magnetic Resonance Imaging*, 37(1):208–216, 2013.

[52] Mette S Olufsen, Charles S Peskin, Won Yong Kim, Erik M Pedersen, Ali Nadim, and Jesper Larsen. Numerical simulation and experimental validation of blood flow in arteries with structured-tree outflow conditions. *Annals of biomedical engineering*, 28(11):1281–1299, 2000.

[53] Gilbert J Perry, Frederick Helmcke, Navin C Nanda, Christopher Byard, and Benigno Soto. Evaluation of aortic insufficiency by doppler color flow mapping. *Journal of the American College of Cardiology*, 9(4):952–959, 1987.

[54] A.N. Smuts, D.C. Blaine, C. Scheffer, H. Weich, A.F. Doubell, and K.H. Dellimore. Application of finite element analysis to the design of tissue leaflets for a percutaneous aortic valve. *J Mech Behav Biomed Materials*, 4(1):85–98, 2011.

[55] David John Wheatley, John Fisher, and David Williams. Heart valve prosthesis, 2001. US Patent 6,171,335.

[56] Fang Li Xiong, Wolfgang A Goetz, Chuh Khiun Chong, Yeow Leng Chua, Stefan Pfeifer, Erich Wintermantel, and Joon Hock Yeo. Finite element investigation of stentless pericardial aortic valves: relevance of leaflet geometry. *Annals of biomedical engineering*, 38(5):1908–1918, 2010.

MOX Technical Reports, last issues

Dipartimento di Matematica
Politecnico di Milano, Via Bonardi 9 - 20133 Milano (Italy)

16/2015   Fumagalli, I.; Manzoni, A.; Parolini, N.; Verani, M.
Reduced basis approximation and a posteriori error estimates for parametrized elliptic eigenvalue problems

15/2015   Taffetani, M.; de Falco, C.; Penta, R.; Ambrosi, D.; Ciarletta, P.
Biomechanical modelling in nanomedicine: multiscale approaches and future challenges

14/2015   Canuto, C.; Nochetto, R.H.; Stevenson R,; Verani, M.
Convergence and Optimality of hp-AFEM

13/2015   Bartezzaghi, A.; Dedè, L.; Quarteroni, A.;
Isogeometric Analysis of High Order Partial Differential Equations on Surfaces

12/2015   Antonietti, P. F.; Beirao da Veiga, L.; Scacchi, S.; Verani, M.
A C^1 virtual element method for the Cahn-Hilliard equation with polygonal meshes

11/2015   Antonietti, P. F.; Marcati, C.; Mazzieri, I.; Quarteroni, A.
High order discontinuous Galerkin methods on simplicial elements for the elastodynamics equation

10/2015   Antonietti, P. F.; Grasselli, M.; Stangalino, S.; Verani, M.
Discontinuous Galerkin approximation of linear parabolic problems with dynamic boundary conditions

06/2015   Perotto, S.; Zilio, A.
Space-time adaptive hierarchical model reduction for parabolic equations

09/2015   Ghiglietti, A.; Ieva, F.; Paganoni, A.M.; Aletti, G.
On linear regression models in infinite dimensional spaces with scalar response

07/2015   Giovanardi, B.; Scotti, A.; Formaggia, L.; Ruffo, P.
A general framework for the simulation of geochemical compaction